PROCEEDINGS A

rspa.royalsocietypublishing.org

Research





Article submitted to journal

Subject Areas:

Fluid mechanics, Computer modelling and simulation, Computational mechanics

Keywords:

Turbulence generation, Wavelets, RANS, Inhomogeneous and anisotropic turbulence, Large spatial variation, Divergence-free

Author for correspondence:

Guang Lin

e-mail: guanglin@purdue.edu

Turbulence Generation from a stochastic wavelet model

Y. Du^1 G. $Lin^{1,2}$

¹School of Mechanical Engineering, Purdue University, West Lafayette, IN 47907, USA

²Department of Mathematics, Purdue University, West Lafayette, IN 47907, USA

This research presents a new turbulence generation method based on stochastic wavelets and tests various properties of the generated turbulence field in both the homogeneous and inhomogeneous cases. Numerical results indicate that turbulence fields can be generated with much smaller bases in comparison to synthetic Fourier methods while maintaining comparable accuracy. Adaptive generation of inhomogeneous turbulence is achieved by a scale reduction algorithm, which greatly reduces the computation cost and practically introduces no error. The generating formula issued in this research could be adjusted to generate fully inhomogeneous and anisotropic turbulence with given RANS data under divergencefree constraint, which was not achieved previously in similar research. Numerical examples show that the generated homogeneous and inhomogeneous turbulence are in good agreement with the input data and theoretical results.

1. Introduction

Turbulence generation has been an important research topic in the study of fluid mechanics for decades. Prior to the emergence of Direct Numerical Simulation (DNS) and Large Eddy Simulation (LES) in fundamental turbulence research, an explicit synthesis scheme was constructed to study turbulence-related phenomena. Kraichnan [16] proposed a divergence-free synthesis method using random wavelets and applied it to diffusion and particle dispersion in Homogeneous Isotropic Turbulence (HIT). Subsequent improvement and modification soon turned it into a viable tool for both theoretical research and acoustic-related computation (Juves [13], Fung et al. [8]). With the increase of computational power, DNS and LES became more practical and successfully enabled people to acquire

© The Authors. Published by the Royal Society under the terms of the Creative Commons Attribution License http://creativecommons.org/licenses/by/4.0/, which permits unrestricted use, provided the original author and source are credited.

greater insights into complex flow phenomena (Rogallo and Moin [26], Moin and Mahesh [21]). Meanwhile, turbulence generation techniques were gradually modified to generate high-fidelity inlet boundary conditions for DNS and LES, as well as interface generation in Detached Eddy Simulation (Spalart [30]), rather than used directly for turbulent flow prediction. The Synthetic Random Fourier Method (SRFM) has become one of the most important methods for inflow turbulence generation.

However, despite its wide application in turbulence-related research, SRFM suffers from several drawbacks. The use of a Fourier basis is not natural for the representation of inhomogeneous turbulence because of its global properties. Although Le et al. [18] proposed a transform to map isotropic homogeneous turbulence generated from SRFM to a general turbulence field with a given Reynolds stress, the transformed turbulence field is no longer incompressible(Wu [32]). Moreover, SRFM uses a set of global Fourier bases for all wavenumbers, which leads to very large computational costs.

At the same time, wavelet noise tools were gradually developed for fluid simulation in the Computer Graphics area and the movie industry. Perlin [22] constructed a widely used turbulence function that could describe the band-limited noise. The form of Perlin Noise was very close to a series of random wavelets. Cook and DeRose [4] rigorously constructed a band-limited wavelet noise upsampling and downsampling procedure. Bridson et al. [2] used Perlin Noise as the vector potential to generate an incompressible flow field. Kim et al. [15] constructed a high-resolution incompressible flow field based on the wavelet noise of Cook and DeRose [4]. As a new mathematical tool developed in the 1980s, wavelets exhibit many delicate and fine properties. Similar to Fourier series, wavelet series can provide a complete basis for the \mathbb{L}^2 function space. Unlike the Fourier transform, which can only extract global frequency (wavenumber) information from functions, the wavelet transform can contain both frequency (wavenumber) and location information, which is an appropriate tool for inhomogeneous turbulence(Farge [6]).

In this research, a turbulence generation method based on stochastic wavelets is developed and tested in both homogeneous and inhomogeneous cases. The turbulence generation method is proposed in Sec.2, including the generation formula, boundary condition treatment, input spectrum and scale reduction algorithm. Numerical results are presented in Sec.3 for both isotropic homogeneous turbulence and fully developed channel flow to validate its accuracy. A comprehensive discussion and analysis of the proposed method are made in Sec.4. A proof for the Reynolds Stress preservation of this method is presented in Sec.5.

2. Methodology

(a) Turbulence Generation Process

(i) Generation of static turbulence field

The model presented in this work provides a way for generating inhomogeneous stochastic turbulent velocity field based on RANS data. Previous research(Shur et al. [28], Lund et al. [20]) has suggested that the fluctuation velocity field could be expressed in the following form:

$$\boldsymbol{u} = \boldsymbol{A} \cdot (\nabla \times \boldsymbol{M}) \tag{2.1}$$

where $\mathbf{u} = (u, v, w)$ denotes the fluctuation velocity. \mathbf{u} is constructed in the manner of equation Eq.2.1 so that the corresponding second order momentum $\langle \mathbf{u}\mathbf{u}\rangle$ is equal to the Reynolds stress tensor. $\mathbf{A}(x)$ corresponds to the Cholesky decomposition of the Reynolds stress tensor $\mathbf{R}(x)$ (Jarrin et al. [12], Shur et al. [28]):

$$R = A^T A \tag{2.2}$$

where A^T denotes the transpose of A. $M = (M_x, M_y, M_z)$ is the vector potential field. The $\nabla \times M$ term is constructed to be divergence free as suggested in Shur et al. [28]. In Kim et al. [15], the

vector potential field was constructed using wavelet noise as described in Cook and DeRose [4]. Similarly *M* is decomposed into a sum of wavelet modes:

$$M(x) = \sum_{|k| \in K} \sum_{x_p}^{N_i} q_{x_p,k} O_{x_p,k} (\omega_{x_p,k} \Psi_k(x - x_p))$$
 (2.3)

Here $x_p = (x_p, y_p, z_p)$ is the position of the wavelet basis in physical space, $k = (k_x, k_y, k_z)$ is the wavenumber corresponding to the wavelet basis, as defined in Perrier et al. [23], and $K = \{l_1, l_2, ..., l_M\}$ is a series of magnitudes of the wavenumber vectors. For each l_i , k is randomly chosen on a sphere of radius l_i in the spectral space. This construction coincides with the nature of the energy spectrum function, i.e. E(l) is the turbulent kinetic energy distributed on a sphere of radius l in the spectral space. x_p is the location of N_i randomly distributed wavelets. The number N_i for each wavenumber l_i is determined using the following expression deducted from uniformly distributed wavelets:

$$N_i = \left[|\Omega| \left(\frac{l_i}{k_0} \right)^3 \right] \tag{2.4}$$

where Ω represents the flow domain. $\omega_{x_p,b}=(\omega^1_{x_p,b},\omega^2_{x_p,b},\omega^3_{x_p,b})$ is a random vector series assumed to be normally distributed with the following statistics:

$$\langle \omega_{\mathbf{x}_n, \mathbf{k}}^i \rangle = 0 \tag{2.5}$$

$$\langle \omega_{\mathbf{x}_p,\mathbf{k}}^i \omega_{\mathbf{x}_p,\mathbf{k}}^j \rangle = \delta_{ij} \tag{2.6}$$

 $\Psi(x)$ is the 3D wavelet basis function constructed using the following tensor-product formulation:

$$\Psi_{k}(x - x_{p}) = \psi(\frac{k_{x}}{k_{0}}(x - x_{p}))\psi(\frac{k_{y}}{k_{0}}(y - y_{p}))\psi(\frac{k_{z}}{k_{0}}(z - z_{p}))$$
(2.7)

From the analytical result in Deriaz and Perrier [5], $\Psi_k(x-x_p)$ in the above form may not provide a complete basis of $\mathbb{L}^2(\mathbb{R}^3)$. However, the basis function above is chosen because of its localization in both physical and spectral space, which offers an appropriate tool for the description and synthesis of turbulence (Farge [6]). A wavelet function with sufficiently high order cancellation is chosen as the 1D wavelet function $\psi(\cdot)$ as stated in Farge [6] and Perrier et al. [23]. k_0 is the Fourier wavenumber of the wavelet function where its Fourier spectrum reaches its peak, i.e.:

$$\mathscr{F}\{\psi(x)\}(k_0) = \max_{k \in \mathbb{R}} \mathscr{F}\{\psi(x)\}(k)$$
(2.8)

The wavelet function $\psi(x)$ is localized in both physical and spectral space, which represents a local structure of the turbulent field with a certain bandwidth of wavenumbers. k_0 , as defined in Eq.2.8, characterizes the most energetic wavenumber of such a local structure. \mathbf{O} in Eq.2.3 is a random rotation matrix in 3-dimensional space, i.e. $\mathbf{O} \in SO(3)$. An efficient way of generating uniformly distributed random rotations is from Stuelphagel [31], where a random rotation matrix is generated by setting:

$$\mathbf{O} = \begin{pmatrix} 1 - 2c_u^2 - 2d_u^2 & 2b_u c_u - 2a_u d_u & 2b_u d_u + 2a_u c_u \\ 2b_u c_u + 2a_u d_u & 1 - 2b_u^2 - 2d_u^2 & 2c_u d_u - 2a_u b_u \\ 2b_u d_u - 2a_u c_u & 2c_u d_u + 2a_u b_u & 1 - 2b_u^2 - 2c_u^2 \end{pmatrix}$$

where a_u , b_u , c_u , d_u are the components of a unit quaterion:

$$a_{u} = \frac{a}{|q|}, b_{u} = \frac{b}{|q|}, c_{u} = \frac{c}{|q|}, d_{u} = \frac{d}{|q|}$$

corresponding to a random quaternion $\mathbf{q} = a + b\mathbf{i} + c\mathbf{j} + d\mathbf{k}$ with coefficients $a, b, c, d \sim N(0, 1)$.

 $q_{x_{n,k}}$ is a series of normalized weights to maintain the local spectrum property of RANS data:

$$q_{\mathbf{x}_p,k} = \sqrt{\frac{E(l)\Delta l}{2k_t c_l}} \tag{2.9}$$

Here E(l) represents the local energy spectrum, which is a known function used as input. A variety of different spectrums can be used as the input spectrum to characterize multiscale features of the turbulence field. Δl is the difference between two neighboring wavenumber magnitudes in K from Eq.2.3. k_t is the turbulent kinetic energy with the following relation:

$$k_t = \int_0^\infty E(l) \, \mathrm{d}l \tag{2.10}$$

The coefficient c_l is determined using a Monte Carlo method:

$$c_{l} = \frac{N_{i}}{|\Omega|} \langle \int_{S} \frac{\partial}{\partial x} \Psi_{k} \, dV \rangle = \frac{N_{i}}{|\Omega|} \langle \int_{S} \frac{\partial}{\partial y} \Psi_{k} \, dV \rangle = \frac{N_{i}}{|\Omega|} \langle \int_{S} \frac{\partial}{\partial z} \Psi_{k} \, dV \rangle$$
 (2.11)

where the ensemble average $\langle \cdot \rangle$ is performed on the random variable k. This ensemble average diverges without restriction on k. In real flow problems, flow domains with finite size can only contain wavelet modes with finitely large support; this prevents any component of k from approaching zero and removes the singularity in Eq.2.11. $S = \operatorname{supp}(\Psi_k)$ is the support set of the tensor-product basis function. It should be noted that depending on the choice of wavelet basis $\psi(\cdot)$, Ψ_k may not be compactly supported, in which case S is the effective support set of function Ψ_k in the numerical sense, which could be defined as follows:

$$S = \{(x, t) | |\Psi_k(x, t)| < \delta\}$$
(2.12)

where δ is a small positive number.

The construction of the system using Eq.2.1, 2.2, 2.3, 2.4, 2.7, 2.9 coincides with the multi-scale and inhomogeneous nature of turbulence, which needs further explanation. It has been stated clearly in multiple literatures that wavelets are good tools for performing energy decomposition to find possible atoms in physical-spectral space(Farge [6], Farge and Schneider [7]). In Eq.2.3 the velocity vector potential M is decomposed into a series of wavelet basis $\Psi_k(x-x_p)$ with its own characteristic wavenumber k and position k_p . Each wavelet mode represents a vortex structure localized both around the position k_p in physical space and the wavenumber k in spectral space. Each k_p is equipped with a random rotation matrix k_p to make sure Eq.2.3 is invariant under rotation. Summation on position k_p indicates a layer of vortices with same magnitude of characteristic wavenumber at different position. The whole fluctuation velocity field is a superposition of layers of local structures with different magnitudes of wavenumbers. The preservation of the Reynolds Stress tensor in the construction of Eq.2.1, 2.2, 2.3 is justified in the Appendix

This construction of the fluctuation velocity field resembles the Synthetic Eddy Methods (SEM) used to generate the inlet flow conditions of LES in previous research (Jarrin et al. [12], Poletto et al. [24], etc.). However, unlike the wavelet functions used in this research, the spectral and physical space properties of functions used to generate structures of different scales in SEM remain unknown. Also, the number of modes with different scales used in eddy synthesis often needs to be determined by experience and tests. Eq.2.4 gives a quantitative representation of the number of wavelet modes in this system, which comes from the density of wavelets used to completely cover each scale in wavelet theory(Hernández and Weiss [9], Deriaz and Perrier [5]). Intuitively speaking, Eq.2.4 indicates that a turbulence field of larger size needs more wavelet modes to cover it. Also, there are much more small-scale structures with higher wavenumber than large-scale structures with lower wavenumber.

Many previous research approaches have constructed the multi-scale system of turbulence using a Fourier basis(Fung et al. [8], Juves [13]), and successfully simulated isotropic homogeneous turbulence from it. However, in general cases of anisotropic inhomogeneous turbulence, such a construction encounters serious problems. Since Fourier bases are global,

covering the whole turbulence field, the construction procedure in Fung et al. [8] is not applicable for generation of turbulence with anisotropy and inhomogeneity. Billson et al. [1], Shur et al. [28] modified a Fourier based reconstruction system so that it could be used to generate inhomogeneous turbulence by multiplying each Fourier basis with a weighting function which quantifies the distribution of turbulent kinetic energy on each scale locally. However, such a modification changes the properties of Fourier basis and causes aliasing between different wavenumbers. In this research, this problem is solved by using random wavelets which are local in both spectral space and physical space rather than a random Fourier basis.

(ii) Generation of dynamic turbulence field

For high Reynolds number turbulence, structures of large and small scales might behave differently according to their own kinematic and dynamic properties; accordingly, they need to be dealt with differently(Pope [25], Fung et al. [8], Lafitte et al. [17]). Large scale contains most of turbulent kinetic energy of the whole turbulence field, while small scale include inertial subrange and viscous subrange. The separation of large and small scales can be achieved by introducing a cutoff wavenumber k_c . However, previous research on turbulence generation indicates that such k_c might be difficult to determine a priori. Here k_c is determined with the following relation:

$$k_c = 2k_e \tag{2.13}$$

where k_e is the wavenumber where the maximum energy spectrum occurs. The magnitudes of wavenumbers in K in Eq.2.3 can be separated into large scales and small scales. For large scales, time advance is achieved by advection induced by the mean velocity field U computed from the RANS model and a random Gaussian advective velocity W_k (Fung et al. [8], Poletto et al. [24]):

$$x_p(t) = x_0 + \int_0^{t'} \mathbf{U}(t') + \mathbf{W}_k(t') dt'$$
 (2.14)

where x_0 is the initial position of a large scale mode. It is reasonable to assume that W_k has a zero mean and a variance equal to that of the velocity field of mode k:

$$\langle \mathbf{W}_{i,k}^2 \rangle = \frac{E(l)\Delta l}{2k_t} \langle u_i u_i \rangle \tag{2.15}$$

where $l = |\mathbf{k}|$, i = 1, 2, 3 represents the three space coordinates and does not imply summation on repeated index.

For small scales structures, Fung et al. [8] and Lafitte et al. [17] suggest that small scale vortices are advected by large scale structures and the mean velocity field. A similar formula as Eq.2.15 can be written as follows:

$$x_p(t) = x_0 + \int_0^{t'} \mathbf{U}(t') + \mathbf{u}_l(t') \, dt'$$
 (2.16)

where u_l represents the large scale velocity field. For the small scale basis, Eq.2.1, 2.2, 2.3 still hold. However, to predict the right Lagrangian decorrelation process, the basis function $\Psi_{x_p,k}$ is modified to the following shape:

$$\Psi_{k}(x - x_{p}, t) = \psi(\frac{k_{x}}{k_{0}}(x - x_{p}))\psi(\frac{k_{y}}{k_{0}}(y - y_{p}))\psi(\frac{k_{z}}{k_{0}}(z - z_{p}))\psi(\frac{\omega_{k}}{k_{0}}t - \phi_{p})$$
(2.17)

where ϕ_p is a random phase, randomly distributed in the support set of the function $\psi(\frac{\omega_k}{k_0}t)$ with uniform distribution. ω_k is a time frequency related to the wavenumber k. Generally, structure with a small wavenumber varies in a slow frequency and vice versa. In the inertial subrange, it is assumed that energy at each wavenumber k is spread over a range of frequency around a characteristic frequency related to the characteristic wavenumber. Thus for each characteristic

wavenumber k a random frequency ω_k is generated with the following distribution:

$$f_{\omega} = \frac{1}{\sqrt{2\pi}\sigma_{\omega}(\mathbf{k})} e^{\frac{-(\omega - \varpi(\mathbf{k}))^2}{2\sigma_{\omega}^2(\mathbf{k})}}$$
(2.18)

where $\sigma_{\omega}(k) = \varpi(k) = \epsilon^{\frac{1}{3}} |k|^{\frac{2}{3}}$ are the variance and mean of the random frequency ω_k (Leslie and Leith [19])

(iii) Incompressible condition modification

The system Eq.2.1, 2.2, 2.3, 2.9 does not satisfy incompressible condition as the result of transformation Eq.2.1. Previous Synthetic Random Fourier Methods(SRFM) all suffer this problem. Some modified SRFM could unify divergence-free constraint, anisotropy and inhomogeneity, but they often involve some special parameter, which largely undermines their generality(Wu [32], Smirnov et al. [29], Huang et al. [10], Castro and Paz [3], Yu and Bai [33]). A slight modification of formulas allows to generate inhomogeneous turbulence field which satisfies divergence-free constraint. The modified formulas are as follow:

$$u = \nabla \times M \tag{2.19}$$

$$M(x) = \sum_{|k| \in K} \sum_{x_p}^{N_i} q_{x_p,k} O_{x_p,k} (\omega_{x_p,k} \Psi_k(x - x_p))$$
 (2.20)

$$q_{x_p,k} = \sqrt{\frac{E(l)\Delta l}{2c_l}} \tag{2.21}$$

$$\langle \omega_{\mathbf{x}_p,\mathbf{k}}^i \rangle = 0 \tag{2.22}$$

$$\langle \omega_{\mathbf{x}_p,\mathbf{k}}^i \omega_{\mathbf{x}_p,\mathbf{k}}^j \rangle = \frac{3}{2} \frac{k_t(\mathbf{x}_p) - \delta_{ij} R_{ij}}{k_t(\mathbf{x}_p)}$$
(2.23)

The system Eq.2.19 to 2.23 is incompressible. Also, it considers the inhomogeneity and isotropy of turbulence field. However, this construction does not preserve full Reynolds stress, only preserves normal Reynolds stress distribution.

(b) Boundary Conditions

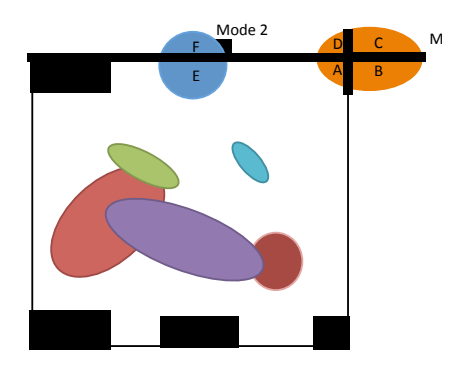
For a large enough flow domain, the boundary conditions for such turbulence generation have no influence on the inner regions away from the boundary. However, in order to retain flow properties near the boundary, modes near the boundary need to be treated differently. For periodic boundaries (Fig.1a), modes on the boundary are separated into different parts and added to the opposite boundaries. Such treatment maintains the exact same velocity value on the opposite boundaries.

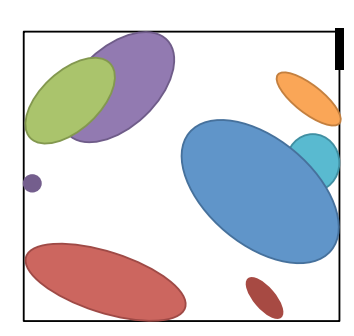
For no-slip boundaries, modes are restricted to the interior of the domain (Fig.1b). In this way, the velocity and second-order moments on the boundary are exactly zero. Also, the characteristic length of modes near the wall boundary is strictly restricted by its distance from the boundary, which automatically creates a damping effect near the boundary.

(c) Input Spectrum

(i) Isotropic case

For high Reynolds number turbulence, the homogeneous isotropic hypothesis is assumed to hold locally. Thus the von Karman-Pao spectrum can be used to obtain spectral information of the





(a) Periodic Boundary

(b) No-slip Boundary

Figure 1: Boundary Conditions: (a) and (b) show the treatment on periodic and no-slip boundaries, respectively. In (a), circles in the plot are supports of different modes. Mode 1 is separated into A, B, C, D parts across the boundary. A stays at its location and B, C, D are shifted to opposite sides (B', C', D'). Mode 2 is separated into E, F parts across the boundary. E stays at its location and E' is shifted to the opposite side (E'). In (b), supports of modes are restricted in the domain so that velocities are exactly 0 on boundary.

turbulence field. The von Karman-Pao spectrum is given by (Juves [13], Saad et al. [27]):

$$E(k) = \alpha \frac{u^{2}}{k_{e}} \frac{(k/k_{e})^{4}}{[1 + (k/k_{e})^{2}]^{17/6}} \exp\left[-2\left(\frac{k}{k_{\eta}}\right)^{2}\right]$$
(2.24)

where $k_{\eta} = \epsilon^{1/4} \nu^{-3/4}$ is the Kolmogorov length scale corresponding to the viscous dissipation length-scale. ϵ is the turbulence dissipation rate from the RANS data. α is determined from normalization of Eq.2.10:

$$\alpha = \frac{55}{9\sqrt{\pi}} \frac{\Gamma(\frac{5}{6})}{\Gamma(\frac{1}{2})} \approx 1.453 \tag{2.25}$$

 k_e is the wavenumber related to the most energetic eddies, could be determined by:

$$k_e = \sqrt{\pi} \frac{\Gamma(\frac{5}{6})}{\Gamma(\frac{1}{2})} \frac{1}{L} \approx \frac{0.746834}{L}$$
 (2.26)

 $L = u'^3/\epsilon$ is the integral length-scale which could be computed from the RANS data.

(ii) Wall turbulence case

Eq.2.20 defines a wavenumber k_e related to the energy containing structures which could lead to a length scale l_e related to k_e :

$$l_e = \frac{2\pi}{k_e}$$

 l_e corresponds to the size of the most energetic eddies. In regions near the wall, l_e should not be larger than double the distance to the wall(Shur et al. [28]):

$$l_e \leqslant 2d_w$$

where d_w is the distance to wall. In regions far away from wall, where damping effect is not important, the expression for k_e returns to the isotropic von-Karman spectrum. Thus a modified expression for k_e which considers the wall effect is as follows:

$$k_e = \max(\sqrt{\pi} \frac{\Gamma(\frac{5}{6})}{\Gamma(\frac{1}{3})} \frac{1}{L}, \frac{\pi}{d_w})$$

(d) Spatial-Spectral decomposition

Eq.2.3 gives a decomposition of the velocity potential field in both physical and spectral space; this allows for a large reduction of the computational cost of reconstruction of the turbulence field, especially for anisotropic inhomogeneous turbulence. Consider a fully developed channel flow, the simulation result of which is shown in Section 3.2(Fig.7). Such a flow is basically 1 dimensional, in which case all turbulence quantities are only functions of y. Eq.2.19 defines the turbulent kinetic energy (TKE) distribution in spectral space, i.e. $E(k, k_t)$. Thus, a spatial-spectral distribution of TKE is defined as follows:

$$E(k,y) = E(k, k_t(y))$$

and satisfies the following normalization condition:

$$k_t(y) = \int_0^\infty E(k, k_t(y)) \, \mathrm{d}k$$

This distribution of channel flow (Fig.2) gives a special insight into the energy distribution and flow structure of the turbulence field. For the majority of the flow field, in regions far away from the wall, most of the turbulent kinetic energy is concentrated in a very narrow area of spectral space which only contributes a small portion of the computational cost in the simulation. In the turbulent boundary layer near the wall, the distribution of the TKE in spectral space becomes very wide and considerably increases computation costs. Based on the generation method from Section 2.1, a scale-reduction algorithm is designed to cut off unnecessary computation while still capturing the energetic structures in the flow field. We define the error e representing the energy loss ratio in order to reduce computational cost:

$$e = 1 - \frac{k_t^e}{k_t}$$

Define two boundary curves $\Gamma_1(y)$, $\Gamma_2(y)$ as follows:

$$\int_{\Gamma_1^e(y)}^{\Gamma_2^e(y)} E(k,y) \, \mathrm{d}k = k_t^e(y)$$

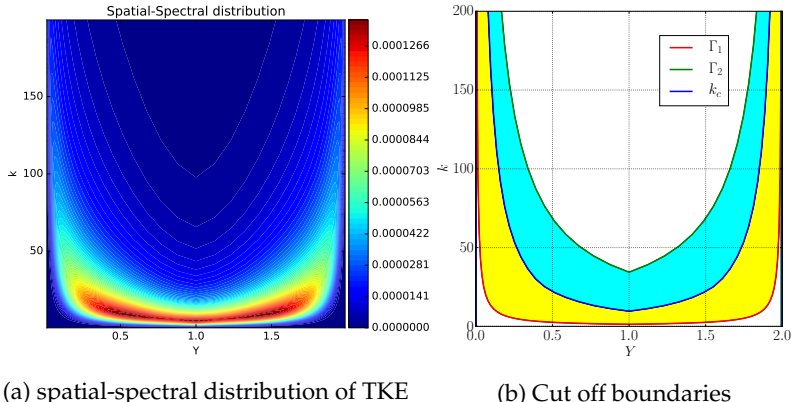
The generation process only needs to be applied in a small band of physical-spectral space (Fig.2) between Γ_1 and Γ_2 to reconstruct most of the TKE up to an error e.

3. Numerical Results

(a) Isotropic homogeneous turbulence

(i) Spatial structure

The generation of isotropic homogeneous turbulence is an important way to validate various properties of turbulence synthesis models. An isotropic homogeneous turbulence case is computed in order to verify the model constructed in the Methodology section. Because the RANS type model cannot compute the k_t and ϵ of isotropic homogeneous turbulence, such data is obtained from previous DNS results (Kaneda et al. [14]). The spectrum of generated turbulence with different modes and different resolutions are compared with the von-Karman



(b) Cut off boundaries

Figure 2: Channel flow: (a) presents the TKE distribution in Physical-Spectral space. (b) shows the regions and cutoff bounds for turbulence generation. The generation process is only conducted in the yellow and blue regions using different time-advance procedures, as proposed in Sec.ii. The yellow part is the large scale generation with smaller wavenumber. The blue part is the small scale with large wavenumber. The white-colored area is discarded in the generation process.

spectrum(Fig.3). The wavenumbers of modes are generated with the following formula(Juves [13]):

$$k_n = \exp[\ln k_0 + nd_k], = 0, 1, 2, \dots M$$

where k_0 is the first wavenumber of the sequence and d_k is a parameter to control the distances between wavenumbers. Another quantity that could be used to examine the spatial structure of the generated turbulence is the structure function defined as follow:

$$D_{11}(r,0,0) = \langle [u(x+r,y,z,t) - u(x,y,z,t)]^2 \rangle$$

$$D_{22}(0,r,0) = \langle [u(x,y+r,z,t) - u(x,y,z,t)]^2 \rangle$$

$$D_{33}(0,0,r) = \langle [u(x,y,z+r,t) - u(x,y,z,t)]^2 \rangle$$

From previous theoretical and experimental research(Fung et al. [8], Ishihara et al. [11], etc.), the second order structure function has the following form in the inertial subrange:

$$D_{11} = D_{22} = D_{33} = C' \epsilon^{\frac{2}{3}} r^{\frac{2}{3}}$$

where C' is a constant. In Fung et al. [8] the value of C' is equal to 1.7. Numerical results of D_{11} , D_{22} and D_{33} are compared with theoretical solutions (Fig.4). The energy spectrum results and second order structural function results indicate that this turbulence generation method gives the right spatial turbulence structure in the homogeneous isotropic cases. The iso-surfaces of the numerical results are shown in Fig.5.

(ii) Time correlation

Eulerian autocorrelation is defined as follow:

$$R_{uu}^{E}(\tau) = \langle u(t)u(t+\tau) \rangle$$

$$R_{vv}^{E}(\tau) = \langle v(t)v(t+\tau) \rangle$$

$$R_{ww}^{E}(\tau) = \langle w(t)w(t+\tau) \rangle$$

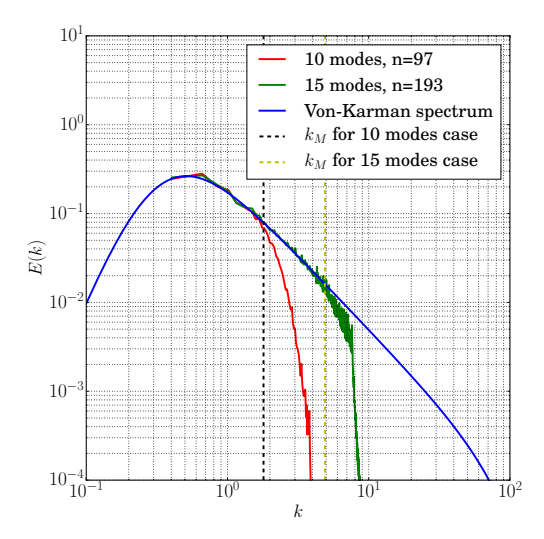


Figure 3: Spectrum of generated turbulence: In this simulation $k_t=0.5$, $\nu=7\times 10^{-4}$, $\epsilon=0.0849$ are nondimensional parameters from previous DNS results. k_{min} is the cutoff wavenumber of the original simulation representing the largest scale. $k_0=0.3$, $d_k=0.2$ for wavenumber generation. The result shows good agreement with the input spectrum within the range of wavenumbers of modes used in the turbulence generation algorithm. As the number of modes increases, the spectrum range that can be accurately captured gets larger. k_M is the largest wavenumber used used in the turbulence generation algorithm. Normally $k_M\leqslant k_N$. k_N is the Nyquist wavenumber of the mesh.

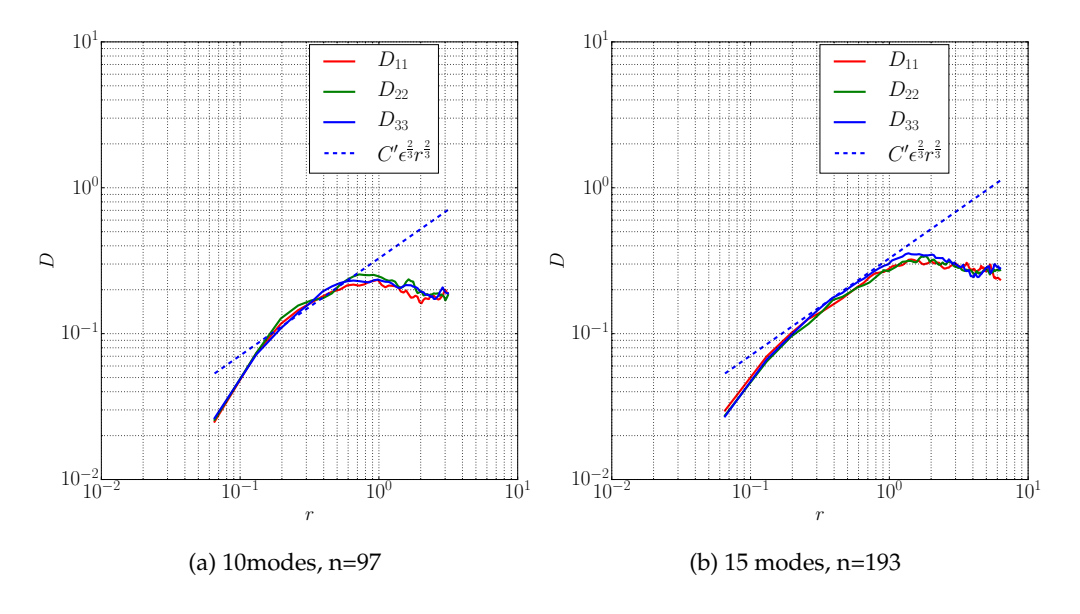


Figure 4: Second order structure functions of simulations with different number of modes and grid points. Dashed lines are theoretical results with constant C' = 1.7. The simulation shows good agreement compared with theoretical results in the inertial subrange.

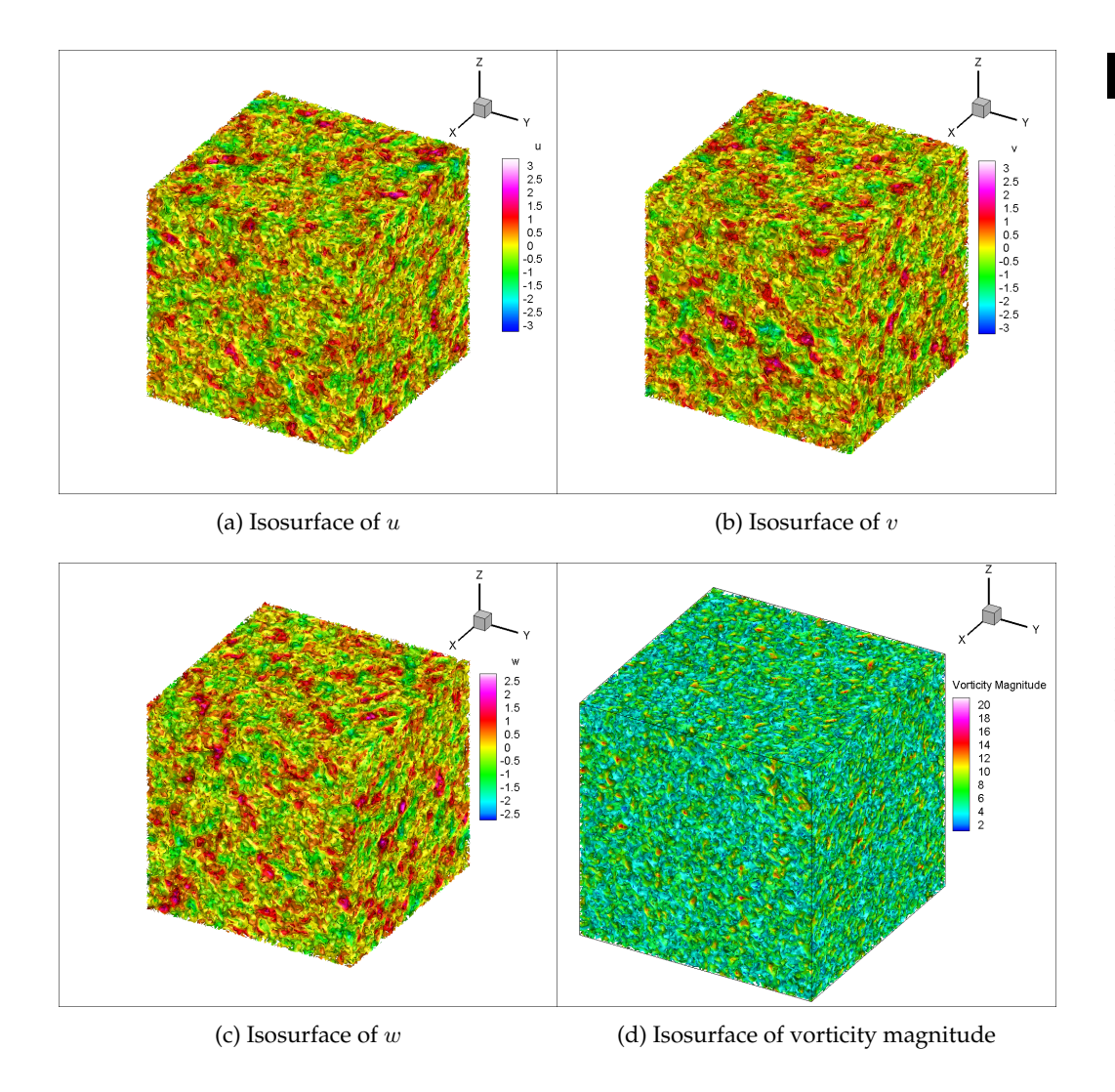


Figure 5: Isosurface results of isotropic homogeneous turbulence generation

Normalized Eulerian autocorrelation can be computed as follow:

$$R_{11}^{E,N}(\tau) = \frac{R_{uu}^{E}(\tau)}{R_{uu}^{E}(0)}$$

$$R_{22}^{E,N}(\tau) = \frac{R_{vv}^{E}(\tau)}{R_{vv}^{E}(0)}$$

$$R_{33}^{E,N}(\tau) = \frac{R_{ww}^{E}(\tau)}{R_{ww}^{E}(0)}$$

Eulerian frequency spectrums are defined as the Fourier transform of Eulerian autocorrelation:

$$\Phi_{uu}^{E}(\omega) = \int_{\mathbb{R}} R_{uu}^{E}(\tau) e^{-i\omega\tau} d\tau$$

$$\Phi_{vv}^{E}(\omega) = \int_{\mathbb{R}} R_{vv}^{E}(\tau) e^{-i\omega\tau} d\tau$$

$$\Phi_{ww}^{E}(\omega) = \int_{\mathbb{R}} R_{ww}^{E}(\tau) e^{-i\omega\tau} d\tau$$

Fung et al. [8], Ishihara et al. [11] suggest that for isotropic homogeneous turbulence the Eulerian frequency spectrum in the inertial subrange can be approximated as follows:

$$\boldsymbol{\varPhi}^E_{uu}(\omega) = \boldsymbol{\varPhi}^E_{vv}(\omega) = \boldsymbol{\varPhi}^E_{ww}(\omega) \approx \boldsymbol{C}^E \epsilon^{\frac{2}{3}} \langle u_1^2 \rangle \omega^{-\frac{5}{3}}$$

where $C^E=0.46$ is a constant from Ishihara et al. [11]. Results of Eulerian autocorrelation and frequency spectrum are shown in Fig.6.

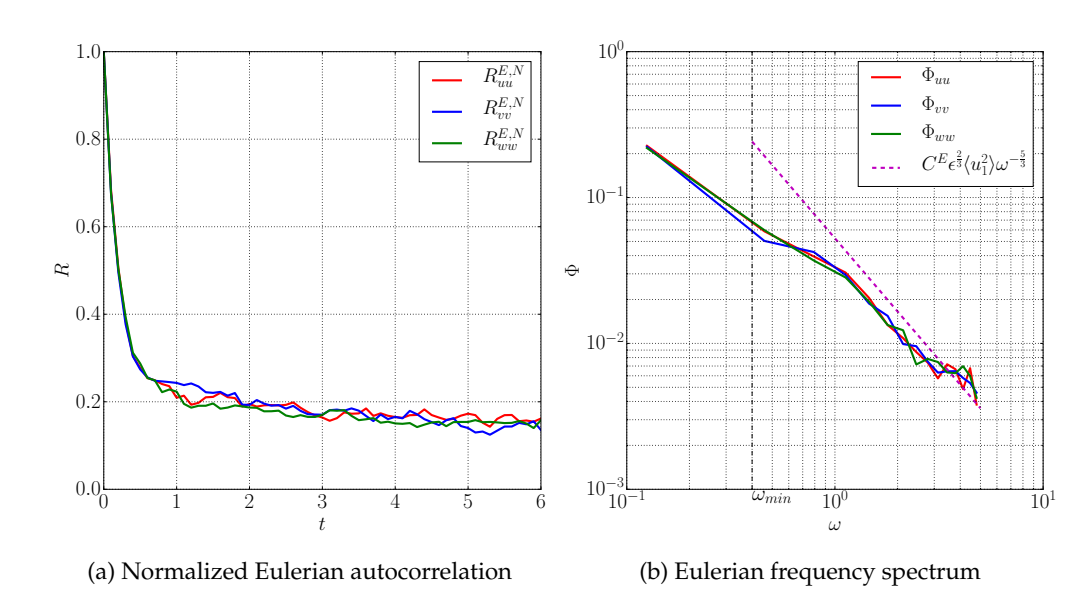


Figure 6: Eulerian temporal and frequency properties of simulation results. Frequency spectrums are compared with analytical results from previous studies. ω_{min} is the lower boundary of the frequency inertial subrange. It can be observed that the Eulerian frequency spectrums of numerical results approximate the theoretical solution in the inertial subrange, especially at the high frequency range.

(b) Fully Developed Turbulent Channel Flow

The RANS data of the channel flow shown in Fig.2 was computed using the Reynolds Stress Model to obtain the full Reynolds stress and turbulence dissipation rate (Fig.7). The turbulent boundary layer was fully resolved, including several grid points in the viscous sublayer. This RANS data is used as input data for turbulence generation. The residual of RSM simulation results are provided in Table.1.

Table 1: Residuals

Equation	Continuity	U momentum	V momentum	n W mome	ntum k equation	
Residual	1.23×10^{-6}	2.04×10^{-6}	7.04×10^{-9}	6.61×10	$^{-9}$ 2.3044×10^{-6}	3
Equation	ϵ	$\langle uu \rangle$	$\langle vv \rangle$	$\langle ww \rangle$	$\langle uv \rangle$	
Residual	5.81×10^{-6}	5.59×10^{-6}	5.72×10^{-6}	5.68×10^{-6}	5.44×10^{-6}	

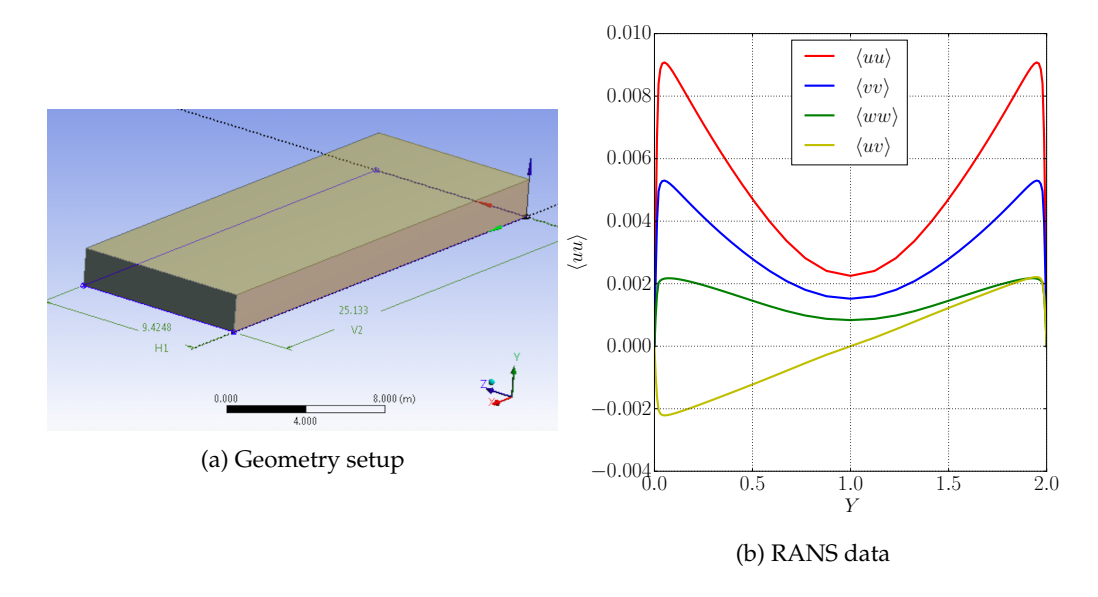


Figure 7: Channel flow: (a) is geometry setup of this channel flow, X is the streamwise direction of the channel flow. Z=0 and $Z=3\pi$ are periodic boundaries. Y=0 and Y=2 are no-slip boundaries. Gradient of mean turbulence field only exist on Y direction, while X and Z direction are uniform. (b) is RANS data of this channel flow from Reynolds Stress Model simulation.

Fig.8 shows the TKE reconstruction at different wavenumbers. It can be observed that most of the turbulent kinetic energy was fully reconstructed except for the very high wavenumber case (k=81.34). Also, for each wavenumber, the energy of generated turbulence fluctuation concentrates in a neighborhood around the wavenumber of specific wavelet basis function, which is a result of Eq.2.7, 2.8. The reconstruction process is done in separated regions because of different time-advance schemes in Section 2.1.2. For k=40.00 and k=81.34, there is a region in which the reconstructed energy is 0. This is due to the fact that the TKE at this wavenumber only contributes to the very small portion of total TKE in this region; thus it is cutoff by the algorithm described in Section 2.4. This portion of the TKE can be accurately reconstructed, but the computation cost will increase significantly and the result does not change much. At very high wavenumbers (Fig.8g, 8h), although the characteristic wavenumber of the wavelet mode is still below Nyquist wavenumber (in this case, $k_N=120$), some part of the energy of the wavelet mode goes beyond k_N , which cannot be captured by the mesh in this case.

Fig.9 shows the comparison of the Reynolds stress from the RANS data and the reconstructed Reynolds stress. It can be observed that the reconstructed $\langle uu \rangle$, $\langle vv \rangle$, $\langle ww \rangle$, $\langle uv \rangle$ agree with the RANS data. It should be noticed that the RANS data used in Fig.9 is slightly different from the data in Fig.7. We define reconstruction ratio as follows:

$$\gamma = \frac{\int_0^{k_N} E(k, y) \, \mathrm{d}k}{k_t(y)}$$

 γ represents the part of the turbulent kinetic energy that could be resolved for the given mesh. The resolvable Reynolds stress $\langle uu \rangle^{\gamma}$ is defined as follows:

$$\langle uu \rangle^{\gamma} = \gamma \langle uu \rangle$$

 $\langle uu \rangle^{\gamma}$ represents the best approximation to the Reynolds stress given a mesh of Nyquist wavenumber k_N . The reconstructed Reynolds stress in Fig.9 shows good agreement with $\langle uu \rangle^{\gamma}$ from the RANS data.

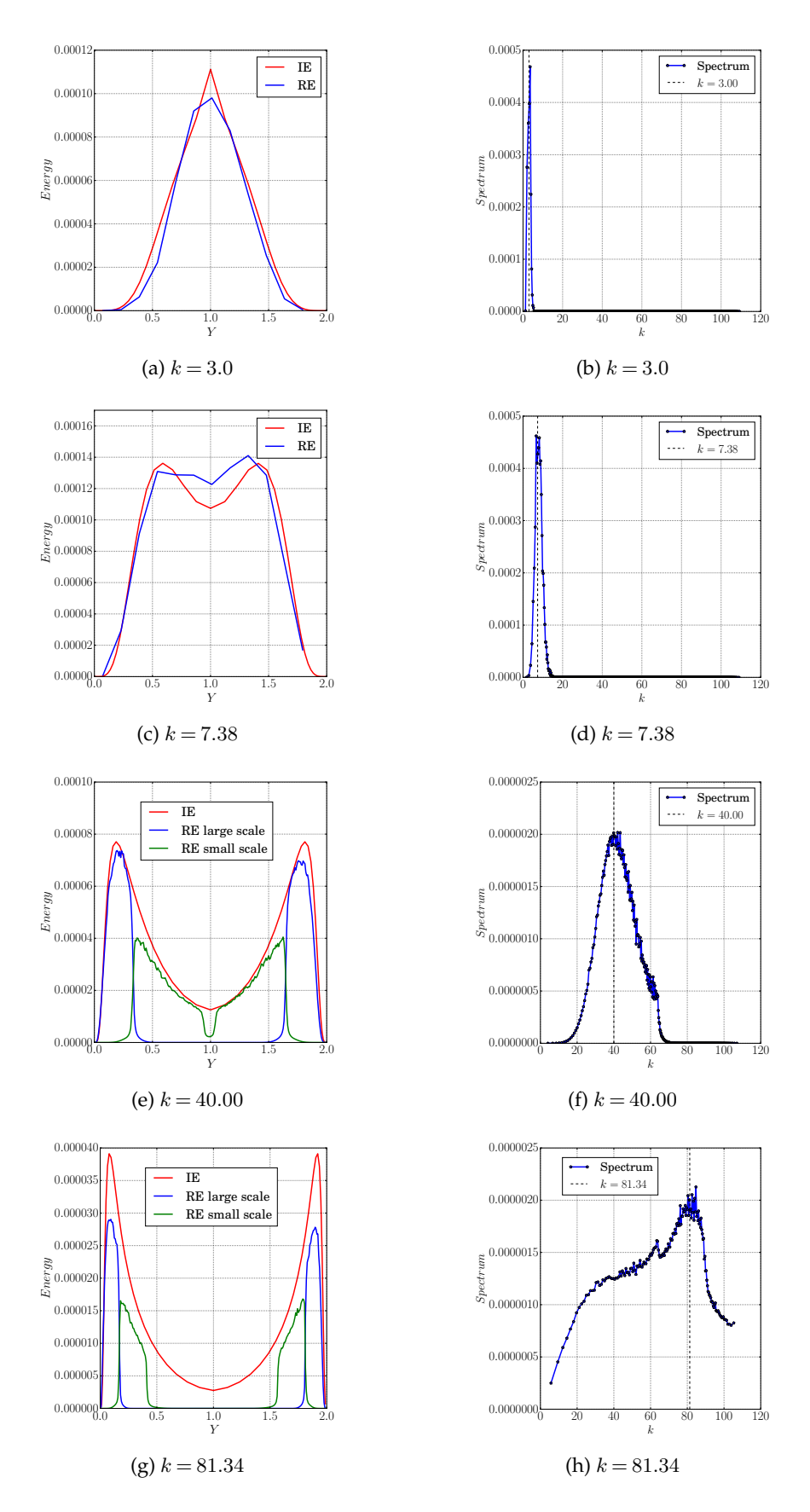


Figure 8: Reconstruction of the TKE at different wavenumbers. Left column: spatial distribution of TKE at certain wavenumbers. Red line: Input energy at certain k. Blue line: reconstructed energy of large scale at k. Green line: reconstructed energy of small scale at k. Right column: spectral distribution of the TKE. IE: Input Energy. RE: Reconstructed Energy.

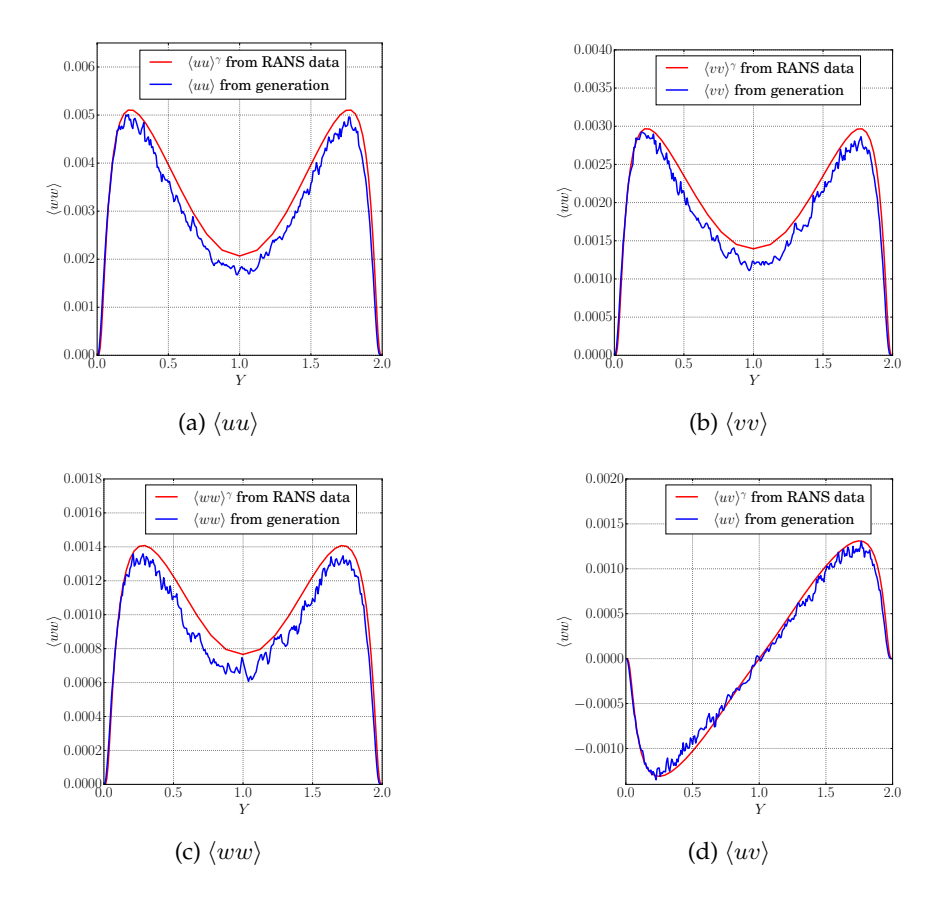


Figure 9: Reconstruction of Reynolds stress distributions: The reconstructed Reynolds stress is compared with resolvable Reynolds stress from the RANS data. The four main reconstructed Reynolds stresses all show good agreement with the resolvable Reynolds stresses.

Iso-contours of 3 total velocity components U, V, W are shown in Fig.10. Large-scale spatial structures are distributed near the centering line of the channel. Near the wall, turbulence structures get smaller and the damping effect of the boundary starts to dominate. The V and W components are close to 0, with some random fluctuation distributed in the cross-section.

4. Conclusion and Discussion

In this paper, a new method of turbulence generation is proposed and evaluated in both the homogeneous and inhomogeneous turbulence cases. Various properties of the generated isotropic homogeneous turbulence show good agreement with both the input data and the theoretical results, including spatial, spectral and frequency properties. The generated fully developed channel flow shows desired spectral and spatial characteristics for different wavenumbers. Preservation of Reynolds Stress for this method is verified through both theoretical deduction and numerical simulation.

Comparison of characteristics of the Stochastic Wavelet Method and SRFM in homogeneous and inhomogeneous turbulence synthesis is listed in Tab.2. The number of modes of different wavenumbers used in turbulence synthesis with Stochastic Wavelet Model is far smaller than that required by SRFM. Also, this new method could fully preserve normal Reynolds stress as well as incompressibility in inhomogeneous and anisotropic turbulence, which could not be achieved with SRFM. Moreover, the computational cost of the Stochastic Wavelet Model could be largely

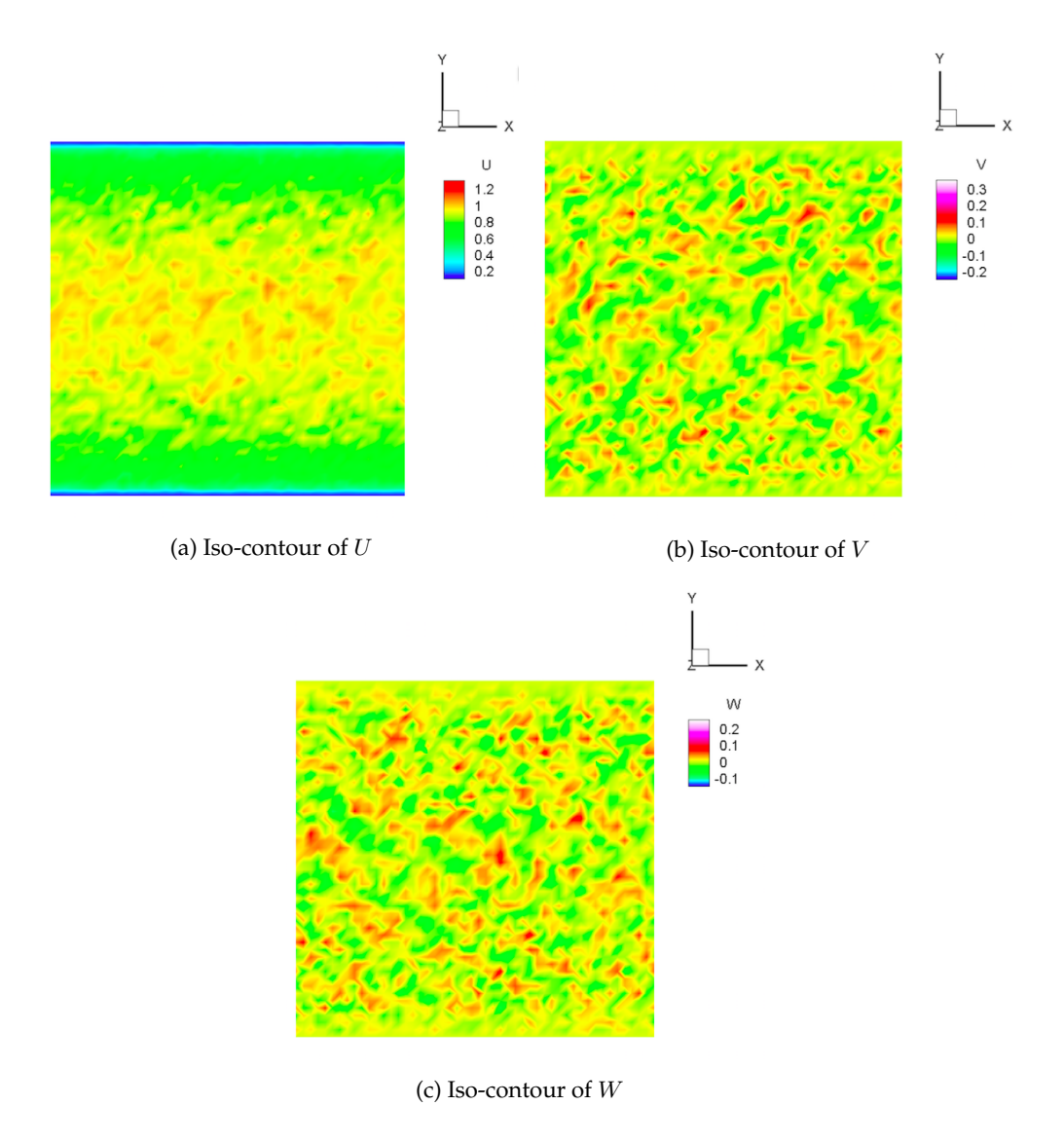


Figure 10: Iso-contour of different total velocity components of generated fully developed turbulent channel flow

reduced without much loss of the turbulent kinetic energy, leading to far less computation cost in comparison with SRFM.

This method exhibits great potential in both scientific computing research and industrial application. Effective and low-cost inlet boundary generation is important for high-fidelity turbulence simulation (DNS, LES) and has become an important research topic recently. In addition, the interface between the RANS region and the LES region in zonal Detached Eddy Simulation also requires turbulence synthesis from RANS data. The Stochastic Wavelet Method proposed in this paper provides a new approach to synthesize turbulence fluctuation fields with desired spectral and statistical properties other than which are not attainable using traditional SRFM under divergence-free constraint. Also, this method could further be applied to Computer Graphics and the movie industry to generate realistic fluid flows in animations with very low computation cost.

	Homogeneous		Inhomogeneous				
	Re_L	Mode Number	Re_{τ}	Reynolds Stress	Incompressibility	Mode Number	
SFRM	723	5000	400	Preserved	Not Preserved	500 - 5000	
SWM	4206	10-20	141900	Preserved	Preserved	15-30	

Table 2: Comparison of SFRM and Stochastic Wavelet Model simulation results

5. Appendix

Consider the turbulence field in a finite domain Ω of size $|\Omega|$. To prove the preservation of the Reynolds stress tensor in scheme outlined by Eq.2.1, 2.2, 2.3, we first prove $v = \nabla \times M$ satisfies:

$$\langle vv \rangle = \underline{I}$$

Proof:

$$\boldsymbol{v} = \nabla \times \sum_{|\boldsymbol{k}| \in K} \sum_{\boldsymbol{x}_p}^{N_i} q_{\boldsymbol{x}_p, \boldsymbol{k}} \mathbf{O}_{\boldsymbol{x}_p, \boldsymbol{k}} (\omega_{\boldsymbol{x}_p, \boldsymbol{k}} \boldsymbol{\varPsi}_{\boldsymbol{k}} (\boldsymbol{x} - \boldsymbol{x}_p))$$

Since curl is a linear operator and is invariant under rotation, we have:

$$oldsymbol{v} = \sum_{|oldsymbol{k}| \in K} \sum_{x_p}^{N_i} q_{x_p, oldsymbol{k}} \mathbf{O}_{x_p, oldsymbol{k}} (
abla imes (\omega_{x_p, oldsymbol{k}} \Psi_{oldsymbol{k}}(x - x_p)))$$

Rewriting the above in index form yields:

$$\begin{split} v_i &= \sum_{|\mathbf{k}| \in K} \sum_{\mathbf{x}_p}^{N_i} q_{\mathbf{x}_p, \mathbf{k}} (\mathbf{O}_{\mathbf{x}_p, \mathbf{k}})_{il} \epsilon_{lmn} \partial_m (\omega_{\mathbf{x}_p, \mathbf{k}} \Psi_{\mathbf{k}} (\mathbf{x} - \mathbf{x}_p))_n \\ &= \sum_{|\mathbf{k}| \in K} \sum_{\mathbf{x}_p}^{N_i} q_{\mathbf{x}_p, \mathbf{k}} (\mathbf{O}_{\mathbf{x}_p, \mathbf{k}})_{il} \epsilon_{lmn} (\omega_{\mathbf{x}_p, \mathbf{k}})_n \partial_m \Psi_{\mathbf{k}} (\mathbf{x} - \mathbf{x}_p) \\ &\langle v_i v_j \rangle = \langle \sum_{|\mathbf{k}_1| \in K} \sum_{\mathbf{x}_{p1}}^{N_i} \sum_{|\mathbf{k}_2| \in K} \sum_{\mathbf{x}_{p2}}^{N_i} q_{\mathbf{x}_{p1}, \mathbf{k}_1} q_{\mathbf{x}_{p2}, \mathbf{k}_2} (\mathbf{O}_{\mathbf{x}_{p1}, \mathbf{k}_1})_{il} (\mathbf{O}_{\mathbf{x}_{p2}, \mathbf{k}_2})_{jr} \\ &\epsilon_{lmn} \epsilon_{rst} (\omega_{\mathbf{x}_{p1}, \mathbf{k}_1})_n (\omega_{\mathbf{x}_{p2}, \mathbf{k}_2})_t \partial_m \Psi_{\mathbf{k}_1} (\mathbf{x} - \mathbf{x}_{p1}) \partial_s \Psi_{\mathbf{k}_2} (\mathbf{x} - \mathbf{x}_{p2}) \rangle \\ &= \sum_{|\mathbf{k}_1| \in K} \sum_{\mathbf{x}_{p1}}^{N_i} \sum_{|\mathbf{k}_2| \in K} \sum_{\mathbf{x}_{p2}}^{N_i} q_{\mathbf{x}_{p1}, \mathbf{k}_1} q_{\mathbf{x}_{p2}, \mathbf{k}_2} \langle (\mathbf{O}_{\mathbf{x}_{p1}, \mathbf{k}_1})_{il} (\mathbf{O}_{\mathbf{x}_{p2}, \mathbf{k}_2})_{jr} \rangle \\ &\epsilon_{lmn} \epsilon_{rst} \langle (\omega_{\mathbf{x}_{p1}, \mathbf{k}_1})_n (\omega_{\mathbf{x}_{p2}, \mathbf{k}_2})_t \rangle \langle \partial_m \Psi_{\mathbf{k}_1} (\mathbf{x} - \mathbf{x}_{p1}) \partial_s \Psi_{\mathbf{k}_2} (\mathbf{x} - \mathbf{x}_{p2}) \rangle \end{split}$$

For $p_1 \neq p_2$ or $k_1 \neq k_2$, $\langle (\omega_{\mathbf{x}_{p1},\mathbf{k}_1})_n(\omega_{\mathbf{x}_{p2},\mathbf{k}_2})_t \rangle = 0$. Therefore:

$$\langle v_i v_j \rangle = \sum_{|\mathbf{k}| \in K} \sum_{\mathbf{x}_p}^{N_i} q_{\mathbf{x}_p, \mathbf{k}}^2 \langle (\mathbf{O}_{\mathbf{x}_p, \mathbf{k}})_{il} (\mathbf{O}_{\mathbf{x}_p, \mathbf{k}})_{jr} \rangle \epsilon_{lmn} \epsilon_{rst}$$

$$\langle (\omega_{x_p,k})_n(\omega_{x_p,k})_t \rangle \langle \partial_m \Psi_k(x-x_p) \partial_s \Psi_k(x-x_p) \rangle$$

Moreover, x_p is uniformly distributed in the flow domain; thus the following holds:

$$\langle \partial_m \Psi_k(x - x_p) \partial_s \Psi_k(x - x_p) \rangle = \langle \int_{\Omega} \partial_m \Psi_k \partial_s \Psi_k \, \mathrm{d}x \rangle$$

By construction (see Eq.2.7), $\partial_s \Psi_k$ is symmetric along all three axes and therefore satisfies:

$$\langle \int_{\Omega} \partial_m \Psi_{\mathbf{k}} \partial_s \Psi_{\mathbf{k}} \, \mathrm{d} \mathbf{x} \rangle = \frac{c_k}{N_i} \delta_{ms}$$

where c_k is defined in Eq.2.11. Noting that $\langle (\omega_{x_p,k})_n(\omega_{x_p,k})_t \rangle = \delta_{nt}$ and substituting into the expression for $\langle v_i v_j \rangle$, we have:

$$\begin{split} \langle v_i v_j \rangle &= \sum_{|\mathbf{k}| \in K} \sum_{\mathbf{x}_p}^{N_i} q_{\mathbf{x}_p,\mathbf{k}}^2 \langle (\mathbf{O}_{\mathbf{x}_p,\mathbf{k}})_{il} (\mathbf{O}_{\mathbf{x}_p,\mathbf{k}})_{jr} \rangle \epsilon_{lmn} \epsilon_{rst} \delta_{nt} \delta_{ms} \frac{c_k}{N_i} \\ &= \sum_{|\mathbf{k}| \in K} \sum_{\mathbf{x}_p}^{N_i} 2q_{\mathbf{x}_p,\mathbf{k}}^2 \langle (\mathbf{O}_{\mathbf{x}_p,\mathbf{k}})_{il} (\mathbf{O}_{\mathbf{x}_p,\mathbf{k}})_{jr} \rangle \delta_{lr} \frac{c_k}{N_i} \\ &= \sum_{|\mathbf{k}| \in K} \sum_{\mathbf{x}_p}^{N_i} 2q_{\mathbf{x}_p,\mathbf{k}}^2 \langle (\mathbf{O}_{\mathbf{x}_p,\mathbf{k}})_{il} (\mathbf{O}_{\mathbf{x}_p,\mathbf{k}})_{jl} \rangle \frac{c_k}{N_i} \\ &= \sum_{|\mathbf{k}| \in K} \sum_{\mathbf{x}_p}^{N_i} 2q_{\mathbf{x}_p,\mathbf{k}}^2 \delta_{ij} \frac{c_k}{N_i} \\ &= \delta_{ij} \sum_{|\mathbf{k}| \in K} \frac{E(l)\Delta l}{2k_t} \rightarrow \delta_{ij} \end{split}$$

as $\Delta l \to 0, l_{max} \to \infty, l_{min} \to 0$. Thus, for enough large K, the following holds:

$$\langle vv \rangle = I$$

From this, it follows that:

$$\langle uu \rangle = \langle (Av)(Av) \rangle$$

= $A(vv)A^T$
= $AA^T = R$

Ethics. This work did not involve any active collection of human data, but only computer simulations.

Data Accessibility. All data used in this manuscript are publicly available on http://www.math.purdue.edu/lin491/data/TGSWM/.

Authors' Contributions. YD conceived the mathematical models, implemented the methods, designed the numerical experiments, interpreted the results, and wrote the paper. GL supported this study and reviewed the final manuscript. All authors gave final approval for publication.

Competing Interests. We report no competing interests.

Funding. We gratefully acknowledge the support from National Science Foundation (DMS-1555072 and DMS-1736364).

Acknowledgements. The authors would like to thank Nickolas D Winovich for proofreading the manuscript.

References

- 1 M. Billson, L.-E. Eriksson, and L. Davidson. Jet noise prediction using stochastic turbulence modeling. In *9th AIAA/CEAS Aeroacoustics Conference and Exhibit*, page 3282, 2003.
- 2 R. Bridson, J. Houriham, and M. Nordenstam. Curl-noise for procedural fluid flow. *ACM Transactions on Graphics (TOG)*, 26(3):46, 2007.
- 3 H. G. Castro and R. R. Paz. A time and space correlated turbulence synthesis method for large eddy simulations. *Journal of Computational Physics*, 235:742–763, 2013.
- 4 R. L. Cook and T. DeRose. Wavelet noise. *ACM Transactions on Graphics (TOG)*, 24(3):803–811, 2005 2005.
- 5 E. Deriaz and V. Perrier. Towards a divergence-free wavelet method for the simulation of 2d/3d turbulent flows. *J. Turbul*, 7(3), 2005.

- 6 M. Farge. Wavelet transforms and their applications to turbulence. *Annual review of fluid mechanics*, 24(1):395–458, 1992.
- 7 M. Farge and K. Schneider. Coherent vortex simulation (cvs), a semi-deterministic turbulence model using wavelets. *Flow, Turbulence and Combustion*, 66(4):393–426, 2001.
- 8 J. C. H. Fung, J. C. Hunt, N. Malik, and R. Perkins. Kinematic simulation of homogeneous turbulence by unsteady random fourier modes. *Journal of Fluid Mechanics*, 236:281–318, 1992.
- 9 E. Hernández and G. Weiss. A first course on wavelets. CRC press, 1996.
- 10 S. Huang, Q. Li, and J. Wu. A general inflow turbulence generator for large eddy simulation. *Journal of Wind Engineering and Industrial Aerodynamics*, 98(10):600–617, 2010.
- 11 T. Ishihara, T. Gotoh, and Y. Kaneda. Study of high–reynolds number isotropic turbulence by direct numerical simulation. *Annual Review of Fluid Mechanics*, 41:165–180, 2009.
- 12 N. Jarrin, R. Prosser, J.-C. Uribe, S. Benhamadouche, and D. Laurence. Reconstruction of turbulent fluctuations for hybrid rans/les simulations using a synthetic-eddy method. *International Journal of Heat and Fluid Flow*, 30(3):435 442, 2009. The Seventh International Symposium on Engineering Turbulence Modelling and Measurements, ETMM7.
- 13 C. B. D. Juves. A stochastic approach to compute subsonic-noise using linearized euler's equations. *AIAA journal*, 1999.
- 14 Y. Kaneda, T. Ishihara, M. Yokokawa, K. Itakura, and A. Uno. Energy dissipation rate and energy spectrum in high resolution direct numerical simulations of turbulence in a periodic box. *Physics of Fluids*, 15(2):L21–L24, 2003.
- 15 T. Kim, N. Thürey, D. James, and M. Gross. Wavelet turbulence for fluid simulation. In *ACM Transactions on Graphics (TOG)*, volume 27, page 50. ACM, 2008.
- 16 R. H. Kraichnan. Diffusion by a random velocity field. The physics of fluids, 13(1):22-31, 1970.
- 17 A. Lafitte, T. L. Garrec, C. Bailly, and E. Laurendeau. Turbulence generation from a sweeping-based stochastic model. *AIAA journal*, 52(2):281–292, 2014.
- 18 H. Le, P. Moin, and J. Kim. Direct numerical simulation of turbulent flow over a backward-facing step. *Journal of fluid mechanics*, 330:349–374, 1997.
- 19 D. Leslie and C. E. Leith. Developments in the theory of turbulence. Physics Today, 28:59, 1975.
- 20 T. S. Lund, X. Wu, and K. D. Squires. Generation of turbulent inflow data for spatially-developing boundary layer simulations. *Journal of Computational Physics*, 140(2):233–258, 1998.
- 21 P. Moin and K. Mahesh. Direct numerical simulation: a tool in turbulence research. *Annual review of fluid mechanics*, 30(1):539–578, 1998.
- 22 K. Perlin. An image synthesizer. ACM Siggraph Computer Graphics, 19(3):287–296, 1985.
- 23 V. Perrier, T. Philipovitch, and C. Basdevant. Wavelet spectra compared to fourier spectra. *Journal of Mathematical Physics*, 36(3):1506–1519, 1995.
- 24 R. Poletto, T. Craft, and A. Revell. A new divergence free synthetic eddy method for the reproduction of inlet flow conditions for les. *Flow, turbulence and combustion*, 91(3):519–539, 2013.
- 25 S. B. Pope. Turbulent flows. IOP Publishing, 2001.
- 26 R. S. Rogallo and P. Moin. Numerical simulation of turbulent flows. *Annual review of fluid mechanics*, 16(1):99–137, 1984.
- 27 T. Saad, D. Cline, R. Stoll, and J. C. Sutherland. Scalable tools for generating synthetic isotropic turbulence with arbitrary spectra. *AIAA Journal*, 2016.
- 28 M. L. Shur, P. R. Spalart, M. K. Strelets, and A. K. Travin. Synthetic turbulence generators for rans-les interfaces in zonal simulations of aerodynamic and aeroacoustic problems. *Flow, turbulence and combustion*, 93(1):63–92, 2014.
- 29 A. Smirnov, S. Shi, and I. Celik. Random flow generation technique for large eddy simulations and particle-dynamics modeling. *Transactions of the ASME-I-Journal of Fluids Engineering*, 123 (2):359–371, 2001.
- 30 P. R. Spalart. Detached-eddy simulation. Annual review of fluid mechanics, 41:181-202, 2009.
- 31 J. Stuelpnagel. On the parametrization of the three-dimensional rotation group. *SIAM review*, 6(4):422–430, 1964.
- 32 X. Wu. Inflow turbulence generation methods. *Annual Review of Fluid Mechanics*, 49:23–49, 2017.

33 R. Yu and X.-S. Bai. A fully divergence-free method for generation of inhomogeneous and anisotropic turbulence with large spatial variation. *Journal of Computational Physics*, 256:234–253, 2014.